

Atomic jets from class 0 sources detected by Spitzer: the case of L1448-C

O. Dionatos, B. Nisini, R. Garcia Lopez, T. Giannini

*INAF - Osservatorio Astronomico di Roma Via di Frascati 33, 00040, Monteporzio
Catone, Italy*

dionatos@oa-roma.inaf.it,
nisini@oa-roma.inaf.it,garcia@oa-roma.inaf.it,giannini@oa-roma.inaf.it

C. J. Davis

*Joint Astronomy Centre, 660 North A'ohoku Place, University Park Hilo, Hawaii 96720,
U.S.A.*

c.davis@jach.hawaii.edu

M. D. Smith

*School of Physical Sciences, Ingram Building, The University of Kent, Canterbury CT2
7NH, U.K.*

m.d.smith@kent.ac.uk

T. P. Ray

Dublin Institute for Advanced Studies, 31 Fitzwilliam Place, Dublin 2, Ireland

tr@cp.dias.ie

M. De Luca

*Indiana University Cyclotron Facility, 2401 N. Milo B. Sampson Lane 47408 Bloomington,
IN U.S.A*

delucama@indiana.edu

ABSTRACT

We present Spitzer-IRS spectra obtained along the molecular jet from the Class 0 source L1448-C (or L1448-mm). Atomic lines from the fundamental transitions of [FeII], [SiII] and [SI] have been detected showing, for the first time,

the presence of an embedded atomic jet at low excitation. Pure rotational H₂ lines are also detected, and a decrease of the atomic/molecular emission ratio is observed within 1' from the driving source. Additional ground based spectra (UKIRT/UIST) were obtained to further constrain the H₂ excitation along the jet axis and, combined with the 0–0 lines, have been compared with bow-shock models. From the different line ratios, we find that the atomic gas is characterized by an electron density $n_e \sim 200\text{-}1000 \text{ cm}^{-3}$, a temperature $T_e < 2500 \text{ K}$ and an ionization fraction $\lesssim 10^{-2}$; the excitation conditions of the atomic jet are thus very different from those found in more evolved Class I and Class II jets. We also infer that only a fraction (0.05-0.2) of Fe and Si is in gaseous form, indicating that dust still plays a major role in the depletion of refractory elements. A comparison with the SiO abundance recently derived in the jet from an analysis of several SiO sub-mm transitions, shows that the Si/SiO abundance ratio is ~ 100 , and thus that most of the silicon released from grains by sputtering and grain-grain collisions remains in atomic form. Finally, estimates of the atomic and molecular mass flux rates have been derived: values of the order of $\sim 10^{-6}$ and $\sim 10^{-7} M_{\odot} \text{ yr}^{-1}$ are inferred from the [SI]25 μm and H₂ line luminosities, respectively. A comparison with the momentum flux of the CO molecular outflow suggests that the detected atomic jet has the power to drive the large scale outflow.

Subject headings: stars: formation — ISM: jets and outflows — ISM: individual (L1448-C) — infrared: ISM — ISM: lines and bands

1. Introduction

The process of mass accretion, leading to the formation of solar type stars, is always associated with mass ejection in the form of collimated jets, which extend from a few AU up to parsecs away from the exciting source. According to the models (Königl & Pudritz 2000; Casse & Ferreira 2000), accretion and ejection are intimately related through the presence of a magnetized accretion disk: the jets carry away the excess angular momentum, so that part of the disk material can move towards the star. This paradigm of star formation is now being observationally tested in Class I and Class II objects through detailed optical and near-IR observations (Ray et al. 2007).

However, the characteristics of jets from these evolved YSOs are unlikely to be appropriate for those from protostars in earlier evolutionary phases, which are expected to propagate in a denser medium and be associated with more energetic mass ejection. In such un-evolved objects, so-called Class 0 sources, the initial part of the jet is often detectable only at mm

wavelengths in the form of a collimated, high-velocity molecular outflow (Gueth & Guilloteau 1999; Lee et al. 2007; Codella et al. 2007). Near-IR H₂ emission is always obscured by high extinction near the central engine and jet base, and instead traces hot gas excited further downstream in bow shocks near or at the jet apex. While it is usually assumed that the molecular jet represents the cold external layer of an embedded atomic jet, in principle the jet could be composed entirely of low excitation molecular gas and this needs to be tested observationally.

Millimeter interferometric observations of high velocity molecular jets from Class 0 sources present characteristics very similar to the hot jets seen in T-Tauri or Class I YSOs, such as a very narrow ($< 2''$) width and a knotty structure resembling that of HH objects (Gueth & Guilloteau 1999; Cabrit et al. 2007). Sub-mm observations in CO and SiO show that such jets are dense, with peak values of $n(\text{H}_2) \sim 10^6 \text{ cm}^{-3}$ (e.g Nisini et al. 2007). Moreover, ISO-LWS observations suggest that they are also warm, with temperatures between 300 and 1500 K inferred from the copious high-J CO and H₂O emission (Giannini et al. 2001). Such a warm gas component may represent the bulk of the mass flux ejected by the protostar, and thus, energetically, may be the jet’s most important component. The very low LWS spatial resolution, however, has not permitted us to draw any conclusions about the detailed structure of this warm gas, giving only physical parameters averaged over the entire outflow.

Spitzer observations now allow us to investigate the properties of the warm gas component of the molecular jet through mid-IR atomic and molecular features probing low excitation gas at $T \sim 100\text{-}2000 \text{ K}$ and $n \sim 10^4\text{-}10^6 \text{ cm}^{-3}$. The moderate IRS spatial resolution (4-20'') allows one to separate, in nearby sources, the inner jet region from the region where the jet is strongly interacting with the ambient medium through bow-shocks.

In this study, we present results of an analysis performed on Spitzer-IRS spectra of the jet from the Class 0 source L1448-C (or L1448-mm). This is a low luminosity ($L=7.5 L_{\odot}$, Tobin et al. 2007) protostellar source located in the Perseus Molecular Cloud ($D \sim 250 \text{ pc}$, e.g. Enoch et al. 2006). A powerful and highly collimated flow is driven by this source, as testified by interferometric CO and SiO maps (Guilloteau et al. 1992; Bachiller et al. 1995). This highly collimated molecular jet is associated with a less collimated and energetic CO outflow, probably representing ambient swept-up material. Near-IR observations performed on the L1448-C outflow show that H₂ hot molecular gas is detected only at the bow shocks at a distance of $\sim 1'$ from the central source; the underlying jet that is responsible for the shocks remains undetected at optical and near-IR wavelengths and has been traced at mm-wavelengths as collimated SiO emission (Guilloteau et al. 1992). Far-IR observations performed with ISO have shown the existence of a warm gas component ($T \sim 1000 \text{ K}$,

$n \sim 10^5 \text{ cm}^{-3}$) associated with the molecular jet, showing up in [OI] $63\mu\text{m}$, H_2 , CO and H_2O pure rotational emission (Nisini et al. 1999, 2000). Recent Spitzer IRAC and MIPS images have shown that the source is actually binary, with a separation of $\sim 7''$ (Jørgensen et al. 2006; Tobin et al. 2007). The north/south binary components are called L1448-CN and CS (Jørgensen et al. 2006) or L1448-mm A and B (Tobin et al. 2007) respectively. We will use the Jørgensen et al. (2006) nomenclature in this paper. Of the two sources, the CN component is associated with the strong millimeter source recognized by interferometric observations as the outflow driving source (Bachiller et al. 1995).

The paper is organized as follows: §2 describes the Spitzer observations and data reduction as well as additional near-IR observations obtained at the UKIRT telescope. §3 and 4 contain our analysis of the observed H_2 and fine structure lines in order to derive the main physical parameters of the jet. Finally, conclusions are presented in §5 .

2. Observations and data reduction

2.1. SPITZER - IRS

The driving source and outflow of the Class 0 object L1448-C were observed with the SPITZER Infrared Spectrograph (Houck et al. 2004) during March and September 2006. Four positions have been targeted with the Short-High (SH), and Long-High (LH) IRS modules ($R \sim 600$, $10\text{-}37\mu\text{m}$) in order to cover the central driving source (L1448-CN), the southern CS source (the position of which spatially coincides with a CO red-shifted clump of Extremely High Velocity (EHV) jet emission named R1 (Bachiller et al. 1990), and two adjacent positions along the blue-shifted part of the jet, that we call OF1 and OF2, the first comprising the B1 mm clump in Bachiller et al. (1990) and the second the H_2 bow-shock, as detected in the near-IR image of the flow by Davis & Smith (1996), respectively (see Figure 1). The plate scale of the detector is $2''.3 \text{ pixel}^{-1}$ and $4''.5 \text{ pixel}^{-1}$ for the SH and LH modules, respectively. Observations with the Short-Low (SL) module ($R \sim 60\text{-}120$, pixel scale $1''.8 \text{ pixel}^{-1}$) were also acquired to extend the spectral coverage down to $5\mu\text{m}$. The observing period was chosen in order to have the SL slit aligned along the L1448 jet. The observations were performed in staring mode with a total integration time of 2.5 hrs per position.

The data were reduced and calibrated with the S13 pipeline. Basic calibrated data (bcd images) were median-combined and cleaned for rogue pixels with the IRSCLEAN_MASK routine, and additional bad pixels in the low resolution module were removed by visual inspection. Spectral extraction was performed with the Spitzer IRS Custom Extraction tool (SPICE). For the high resolution modules the full slit was extracted, whereas for the SL mod-

ule the full slit length was divided into four equal regions ($\sim 14''$) that were consecutively extracted in order to best match the high resolution module pointings. High resolution spectra were defringed using the IRSFRINGE package while the zodiacal light contribution was estimated using the Spitzer Planning Observations Tool (SPOT) and subtracted. Inter-order flux offset and curvature effects were minimized by optimally selecting the best approximation between the point and extended source calibration options (SPICE), according to the morphology of each observed region. The resulting line flux difference between the two extraction methods is $\sim 20\%$ which can be considered as an upper limit to the error for the observed line fluxes.

The calibrated spectra combined for all modules at each position are presented in Figure 2; in the same figure open squares and triangles represent IRAC bands 3,4 and MIPS band 1 continuum flux measurements from the recent studies of the region by Jørgensen et al. (2006) and Tobin et al. (2007) respectively. Their good agreement with the extracted spectra baseline confirms the appropriateness of the adopted extraction and calibration techniques. In particular, the procedure for zodiacal light subtraction is sufficiently precise to cancel the baseline jumps between different modules, the only exception being the SH and LH modules at the CS position, around $20\mu\text{m}$.

The extracted spectra display a number of emission lines that arise both from molecular and forbidden atomic or ionic transitions. Line identification has been performed considering the features lying more than 3σ above the local rms and whose emission peak, fitted by a gaussian, is within half a resolution element from the theoretical vacuum wavelength. The observed molecular emission lines are due to H_2 , where the full series of pure rotational transitions (S(0) - S(7)) in the given wavelength range of the instrument are detected. Atomic and ionic emission has been detected in the form of the fundamental fine-structure lines from [FeII] ($25.98\mu\text{m}$), [SI]($25.25\mu\text{m}$) and [SiII] $34.81\mu\text{m}$ (see Fig.3). None of the other numerous higher excitation [FeII] lines falling in the investigated wavelength range has been detected at the 3σ level: this fact, combined with the non-detection of the [NeII] line at $12.8\mu\text{m}$, already suggests that the investigated region presents very low excitation conditions.

In addition to emission lines, wide absorption bands are also observed in the spectra extracted at the two sources, the most prominent being those due to silicates at $9.7\mu\text{m}$, water ice at $6.02\mu\text{m}$ and CO_2 ice at $15.2\mu\text{m}$.

Fluxes of the individual lines were computed by gaussian fitting after subtracting a sloped baseline within the Spectroscopic Modeling, Analysis and Reduction Tool (SMART) (Higdon et al. 2004). In Table 1 we report the parameters of the detected lines, along with their identified transitions and the associated rms errors given by the 1σ uncertainty derived from the fluctuations of the local baseline. The measured fluxes have a larger uncertainty of

up to 20% given by the flux calibration uncertainty. The 0–0 S(2) line has been observed by both the SL and SH modules. The line fluxes measured in the two modules agree inside the errors with the exception of the position OF2, where the SH module gives a flux higher by a factor of two. This difference could be due to a different bow-shock area sampled by the two modules. For consistency, we use in all the positions the average of the two measurements.

In the same table we also give the upper limits for a set of non-detected lines that fall within the observed range and that will be used in the analysis that follows. In a previous study of the same region with ISO/SWS, Nisini et al. (1999) detected the S(3) to S(5) H₂ transitions in a region of 14'' × 27'' centered on the L1448-C source. The derived fluxes are a factor between 3 and 8 larger than the ones presented here. The FOV of the SWS observations is around 10 times larger than the region extracted in our spectra: therefore the observed flux difference can be attributed to the different adopted apertures.

2.2. UKIRT - UIST

In order to further investigate the excitation conditions along the jet axis, additional spectra, covering the wavelength range from 1.4 to 2.5 μm, were obtained on 4th October 2006 at UKIRT (UK Infrared Telescope) using the image-spectrometer UIST in spectroscopic mode. A 4-pixel-wide slit was used with a pixel scale of 0.12'', corresponding to a spectral resolution ~ 500-700. The slit was positioned roughly parallel with the jet axis and thus aligned with the SL IRS slit, at a position angle (PA) of -17°. Object-sky-sky-object sequences were made with a total exposure time of 300s for each one. Each spectral image was bias subtracted and flat-fielded using the ORAC data reduction software. Further reduction was performed using IRAF standard tasks. An Argon lamp was used in order to wavelength calibrate the spectra. B-type stars were observed with the same configuration in order to remove the telluric features and flux calibrate the spectra. Once the reduction was completed, the APALL IRAF task was used to extract the spectra corresponding in length to the four regions investigated with IRS. Table 2 lists the lines detected in the CN, OF1 and OF2 regions, with the corresponding measured flux. No lines have been detected in the CS position. Only H₂ 1-0 and 2-1 ro-vibrational lines were detected, while any atomic or ionic emission (e.g. the strong [FeII] lines at 1.25 μm and 1.64 μm) is missing, as already evidenced by Caratti o Garatti et al. (2006). It can be noted that in the OF2 position, which corresponds to the bow-shock position, a large number of transitions from higher excitation 1-0 lines (up to S(9)) are detected. This may be indicative of higher excitation conditions associated with the bow-shock or lower reddening pertaining to this region since it is located far from the mm source core.

3. Analysis of the excitation conditions along the jet

3.1. Extinction and spatial variation of line luminosity

Optical extinction (A_V) values along the line of sight of the CS and CN sources have been measured from the $9.7\mu\text{m}$ silicate absorption feature, adopting the relationship between the optical depth of this feature and the visual extinction given by Mathis (1998), i.e. $A_V/\tau_{9.7}=19.3$ mag. The derived A_V values are 32 and 11 mag for the CS and CN source, respectively. In the OF1 and OF2 positions no silicate absorption is detected so no direct measurement of A_V from our spectra is possible. We have therefore assumed an extinction of 5 mag, as derived by Nisini et al. (2000) towards the direction of the B1 clump (coincident with the OF1 position). Such a low value of extinction is in agreement with the absence of water and CO_2 ice absorption features in the spectra of these positions, as these features should become detectable in the Spitzer spectra only once the visual extinction reaches values above 4.3 ± 1.0 mag (Whittet et al. 2007). All the individual detected lines have been dereddened adopting these A_V values and the different extinction laws appropriate for the considered wavelength ranges: in the range from 1 to $13\mu\text{m}$ the extinction law of Rieke & Lebofsky (1985) was adopted while from 13 to $23\mu\text{m}$ the extinction law of Mathis (1998) was used, which was extrapolated to $28\mu\text{m}$.

An a posteriori check of the correctness of the adopted extinction values was done using the Boltzmann diagrams constructed from the H_2 near and mid-IR lines (see Sect. 3.2), by examining the fit to a straight line of transitions appropriate for the $9.7\mu\text{m}$ silicate absorption (like the 0–0 S(3) line at $9.67\mu\text{m}$) and at the interface between the near- and mid-IR lines in the same plot.

Once extinction corrected, we have explored the spatial variation of the relative atomic/molecular emission, by plotting the ratio of the [FeII] $26\mu\text{m}$ and [SI] $25\mu\text{m}$ with respect to the H_2 0–0 S(1) line (Figure 4). This plot clearly shows that the relative brightness of the atomic component with respect to the molecular component sharply decreases going from the CN to the OF1 position while only slightly increasing again at the bow shock position. A similar behavior has been observed in the near-IR for a number of Class I jets, where the atomic and molecular components have been traced by the [FeII] $1.64\mu\text{m}$ and H_2 1–0 S(1) lines respectively (Nisini et al. 2002, 2005). In these sources, the relative decrease of atomic gas emission with respect to H_2 in the jet beams is accompanied by a decrease of excitation in the jet which occurs on scales of $\sim 5\text{--}10''$ from the driving source. The interpretation of this behavior is that the jet, heated and ionized in the acceleration region, progressively expands and cools down until it strongly interacts with the medium through a bow shock. The spatial scale of the IRS instrument is too poor to resolve the intensity and excitation variations within the

jet expansion region; a qualitative inspection, however, suggests a similar behavior, in spite of the different physical conditions pertaining to the L1448 jet.

3.2. H_2 emission

Being very easily thermalized, H_2 lines can be used as probes for the temperature by means of excitation diagrams. The latter are constructed by plotting the values of $\ln(N_{v,J}/g)$ against $E_{v,J}$, where $N_{v,J}$ is the column density for the population at the upper level, $E_{v,J}$ and g are the level energy and statistical weight. Assuming LTE conditions, these two quantities are linearly related, and the local temperature can be derived from the slope of the fit. We have constructed excitation diagrams in each position combining the Spitzer and UKIRT observed lines. For these, column densities have been derived dividing the line flux for the aperture adopted for the spectral extraction, assuming that the emission is extended and fills the extraction apertures in a uniform way. This cannot be the case for the 0–0 S(0) line observed with the much larger aperture of the LH module: the H_2 fundamental transition should be in fact also affected by diffuse emission from the cloud, therefore the derived column density can be considered as an upper limit of the S(0) column density in the jet. In constructing the Boltzmann diagrams, we have assumed an H_2 ortho/para ratio equal to the equilibrium value of 3. We do not appreciate significant variations from this value inside the errors of the data-points.

The excitation diagrams for each position are presented in Figure 5; in these, Spitzer (open circles) and UKIRT lines (open squares) are least square fitted with a straight line. The visual extinction values used and temperatures derived from the slope of the fitted lines are displayed in the top right of each diagram. In all cases, data points are reasonably well aligned and thus giving support to the assumption of a H_2 gas in LTE. Because of the high values of visual extinction at CS, the lack of data points results in a fit with large uncertainties in the derived temperature.

Given the fact that the lines falling within the Spitzer and UKIRT ranges originate from pure rotational and ro-vibrational transitions, respectively, the two sets of lines may trace different temperature regimes. However it is only in the bowshock position that the two sets of lines clearly trace two different temperature components. In the other positions, the extinction corrected upper limits on high excitation H_2 lines suggest that a single temperature component with T ranging between 600 and 900 K, well represents the excitation conditions. It is only in the OF1 position that the column density of the S(6) and S(7) lines deviate from the single temperature fit: we think that the displacement of these lines is not reliable, since such curvature is not followed by the NIR measurements of the higher excitation lines.

From the Boltzmann diagrams it is also possible to derive the total H_2 column density of the warm gas, from the intersection of the fitted line to the data points and the abscissa of the excitation diagram, which is equal to $\ln N(H_2)/Q(T)$, with $Q(T)$ is the partition function at temperature T .

The derived temperatures and column densities for each of the observed regions are presented in Table 3. The gas temperature shows a slight decrease going from the driving source (CN) to the OF1 position, while column density displays a constant increase from the CS to the OF2 positions. This trend confirms that the excitation conditions decrease as the jet propagates into the ambient medium, and that in the inner region the jet is mostly atomic, as testified from the $[FeII]/H_2$ ratio displayed in Figure 4.

3.2.1. Shock model

As seen in the previous section, the H_2 Boltzman diagram in the OF2 position shows the presence of different temperature components, likely arising in the unresolved cooling zone behind the bow shock. In order to constrain the shock conditions from our Spitzer and UKIRT observations, we have attempted to model the derived H_2 column densities with a C-type bow-shock model (Smith 1991). For a better comparison of the derived column density with the model fit, we have constructed a Column Density Ratio (CDR) plot, in which the column density in the upper energy level of each transition has been normalized to the value given by a gas at 1000K. These values are then presented relative to the column of the 1-0 S(1) upper energy of 6953K (see Fig. 6). In this Figure, triangles represent Spitzer 0-0 lines, squares represent all lines originating from the first vibrational levels, including the 1-1 upper limits derived from the Spitzer IRS spectra, and diamonds correspond to 2-1 lines; model predictions are superimposed over the data. The predicted column densities are calculated assuming that the upper energy levels are in rotational LTE but vibrationally in non-LTE. This is a reasonable assumption for the levels at low excitation energy, while the higher rotational levels appear to switch across from the 1-0 line to the 2-1 values, indicating that this assumption probably does not hold anymore for the higher levels. The best fit model prediction is obtained with a bow shock moving at 100 km s^{-1} into a medium of (H nucleon) density 10^5 cm^{-3} . The ion fraction of 10^{-6} and magnetic field strength, corresponding to an Alfvén speed of 2 km s^{-1} , imply that the non-dissociative wings of the bow are C-type shocks. The bow geometry required for the obtained fit is such that the bow must possess a compact apex and extended flanks with a shape $Z \propto R^s$ with $s = 1.38$ in cylindrical coordinates. Then, a large column of low excitation gas is generated by the bow. A C-bow shock model with similar parameters as adopted here was able to reproduce also the kinematic and the

1-0 S(1) morphology of the considered bow shock (Davis & Smith 1996).

3.3. Atomic Jet

As pointed out in Section 2.1, the detection of only the fundamental [FeII] transition indicates that the excitation conditions of the atomic jet are very low. The [FeII] 26 μm line originates from the ${}^6D_{7/2}$ level, that has an excitation temperature of ~ 550 K, while the level just above this one, ${}^6D_{5/2}$, gives origin to a transition at 35 μm , having $T_{ex} \sim 960$ K. In principle, the non detection of the 35 μm transition could give a strong constraint on the gas temperature. However, the spectral region around 30 μm is very noisy and the upper limits are not stringent. To get constraints on the temperature, we have instead considered the upper limit on the ${}^4F_{7/2} - {}^4F_{9/2}$ transition at 18 μm , that lies in a region of lower noise. In addition, we have also used the ratio [SiII]35 μm /[FeII]26 μm as a density probe. Si and Fe have a comparable ionization potential (8.15 and 7.9 eV respectively) thus a similar degree of ionization. Furthermore these two lines are excited at a similar temperature of ~ 500 K, thus their ratio depends only on the electron density and on the [Si/Fe] gas phase abundance ratio. We assume a [Si/Fe]_{gas} ratio equal to the solar ratio (taken from Girart & Acord 2001), an assumption implying that the two species are equally depleted on grains. The validity of this assumption is further examined in Section 4.

Figure 7 presents a plot of the [SiII]34.8 μm /[FeII]26.0 μm ratio as a function of the electron density, for temperatures of 1000K and 2000K (solid and dashed lines). This diagram has been constructed employing a statistical equilibrium model that considers the first 16 levels for [FeII] (Nisini et al. 2002), and a two level system for [SiII]. Radiative and collisional rates for the [SiII] have been taken from Dufton & Kingston (1991). Hatched areas represent the ratios observed in the CN and OF2 regions, respectively. Such observations are consistent with values of n_e in the range ~ 300 -500 for the OF2 position and ~ 200 -1000 cm^{-3} for the CN position.

In Figure 8, the upper limit ratio [FeII] 18 μm to 26 μm is plotted as a function of the gas temperature, for different electron density values. The 26 μm line flux and the 18 μm line upper limit have been measured on two IRS modules having different field of views and therefore their intrinsic ratio depends upon the extension of the emitting region. A conservative upper limit on this ratio is obtained assuming beam filling and consequently normalizing the line ratio to the different field of view. The upper limits obtained in this way are displayed in Fig. 8 for the CN and OF2 regions. From this plot, we derive that gas temperatures less than ~ 2500 K and ~ 1500 K are responsible for the emission observed in the OF2 and CN positions, respectively.

The derived physical conditions significantly differ from the conditions measured from [FeII] near-IR lines in jets from more evolved class I sources, that have temperatures ranging from 7000 and 15000 K and densities $\sim 10^4$ - 10^5 cm $^{-3}$ (e.g. Nisini et al. 2002; Takami et al. 2004) . Low electron density values, in particular, point to a low ionization fraction for the gas under consideration. Total n_{H_2} densities of the order of 10^5 cm $^{-3}$ or higher have been inferred in the L1448 jet from sub-mm and far-IR observations (Nisini et al. 2000, 2007), implying a ionization fraction x_e of $\sim 10^{-2}$ or lower.

The inferred low temperature and ionization fraction, in conjunction with the non-detection of the [NeII] 12.8 μ m line, imply that, if these lines are shock excited, the shock velocity should be low. Fast *J*-type shocks (e.g. Hollenbach & Mc Kee 1989) are therefore excluded. Low-velocity *J*-type shocks might provide sufficient ionization to excite the fundamental ionic fine-structure lines, but the shock velocity needs to be lower than ~ 10 km s $^{-1}$ to have a temperature of less than ~ 2000 K.

Part or all of the atomic emission observed on-source may in principle also originate from excitation in a circumstellar disk. Line emission disk models (Gorti & Hollenbach 2008) as well as Spitzer observations in T Tauri disks (e.g. Pascucci et al. 2007, Lahuis et al. 2007) show however that disk emission is characterized by both strong [NeII] 12.8 μ m, excited in the high temperature gas heated and ionized at the disk surface, and [FeI] 24 μ m line, originating in the deeper disk vertical layers, that we do not detect here.

The strong atomic emission observed on-source may instead originate from the jet base, in a zone similar to the Forbidden Emission Line (FEL) regions observed in Class I/II jets although with very different excitation conditions (e.g. Davis et al. 2003). In analogy with the FEL regions there is a decrease in intensity of the atomic emission with distance from the source, likely caused by the expansion of the jet and the consequent cooling down of the gas.

4. Dust disruption and abundance of refractory species

Gas phase abundances of Iron and Silicon are very low in the interstellar medium since these refractory elements are easily depleted onto the cores of dust grains. Shocks occurring along the outflows of young stars are able to at least partially restore the refractory elements to the gas phase, through processes like sputtering and grain-grain collisions (Jones 2000). Observations of mm and sub-mm SiO lines in many molecular outflows (e.g. Codella et al. 2007; Gibb et al. 2007; Nisini et al. 2007) have shown that dust grains are indeed partially destroyed, and that the released Si undergoes chemical reactions leading to the formation

of SiO. (Schilke et al. 1997; Gusdorf et al. 2008). SiO abundance determinations along the molecular jet of L1448 show however that gas-phase Si locked in SiO is only about $5 \cdot 10^{-3}$ of the Si solar abundance: thus either not all of the Si released by the dust reprocessing is converted into SiO, or the shocks are not able to completely restore all the Si to the gas phase. The detection of the [SiIII] fundamental line in our spectra suggests that indeed a significant part of gas-phase Si is present in ionic form. On the other hand, the gas-phase abundance of Fe in jets have been so far measured only in near-IR jets of Class I sources, from the bright near-IR [FeII] lines (Nisini et al. 2002, 2005; Podio et al. 2006). Such studies have shown that a large fraction of Fe (from 70 to 95%) is still locked in grains, indicating that dust grains have not been totally destroyed by shocks. No estimates have been so far given about the iron gas-phase abundance in Class 0 molecular outflows. We can now provide abundance estimates of both Si and Fe through the detected emission lines of their single-ionized atoms.

The gas phase abundance of refractory elements can be derived from a comparison of their emission lines with those of a non-refractory species emitted under the same physical conditions. In the case of our spectra, the [SI]25.2 μ m line can be used as a reference, as sulfur is not depleted in grains, assuming that all the sulfur is in neutral form. To check this hypothesis, we have computed the S⁰/S⁺ ratio applying ionization equilibrium between collisional and charge-exchange ionization, and direct/dielectronic recombination (rates from Stancil et al. 1998; Landini & Monsignori Fossi 1990). For the inferred physical conditions of $T \sim 1000$ -2000 K and $x_e \lesssim 10^{-2}$, it results that 95% of S is in neutral form. The iron gas phase abundance, relative to the solar value, can be therefore written as:

$$[Fe]_{gas}/[Fe]_{\odot} = \frac{[Fe/S]}{[Fe/S]_{\odot}} = \frac{F([FeII]26\mu m)}{F([SI]25.2\mu m)} \times \frac{\epsilon([SI]25.2\mu m)}{\epsilon([FeII]26\mu m)} \times [S/Fe]_{\odot} \quad (1)$$

where $\epsilon([SI]25.2\mu m)$ and $\epsilon([FeII]26\mu m)$ are the theoretical emissivities, $[Fe/S]_{\odot}$ is the solar abundance ratio, taken from Asplund et al. (2005), and $F([FeII]26\mu m)/F([SI]25.2\mu m)$ is the observed ratio. A similar expression can be written for the $[Si]_{gas}/[Si]_{\odot}$ ratio. To compute the theoretical emissivities, we have considered for S a 5 level statistical equilibrium code assuming electronic collisional excitation and $n_e=400 \text{ cm}^{-3}$. Two values of temperatures have been considered: 2500 K (the upper limit derived in the OF2 position) and 600 K (the lower value derived by the H₂ analysis). In a medium with high total density and low ionization fraction, such as the one we are considering here, collisions with atomic hydrogen may become important in the excitation of atomic species such as [SI], in spite of the low n_H collisional de-excitation rates with respect to the rates for electronic collisions ($\gamma_H/\gamma_e \sim 10^{-4}$ for the [SI]25 μ m line, Hollenbach & McKee (1989)). In order to asses how collisions with

hydrogen affect the results, we have calculated the emissivities also assuming a medium with a total density of 10^5 cm^{-3} and $n_H = 0.1 n_{tot}$ ¹.

We have applied the above analysis to the values observed in the CN, OF1 and OF2 positions: for the [SI]25.2 μm flux, we have taken the average value given by the determinations obtained in the two different orders of the LH module. Results are summarized in Table 4: the uncertainty in temperature results in a factor of two the uncertainty in derived abundances, while a difference of four is found between results obtained assuming collisions with electrons and with atomic hydrogen.

The Table shows that the gas phase abundance of Fe and Si remains between 5 and 20% of the solar values for both species and in all positions. Similar low values of Fe abundances have been also found in the inner regions of jets from Class I sources, from the analysis of the [FeII] NIR lines (Nisini et al. 2005; Podio et al. 2006), while larger abundances (from 20 to 70% of the solar value) have been derived at large distances from the driving source and in bow shocks (Nisini et al. 2002; Giannini et al. 2008).

Finally, taking a SiO abundance of $5 \cdot 10^{-3}$ derived by Gusdorf et al. (2008), the Si/SiO abundance ratio is ~ 100 , giving support to the hypothesis that most of the silicon released from grains remains in atomic form.

5. Mass and mass flux in the warm gas

The presented observations point to the presence of warm gas associated with the L1448 CO and SiO millimeter jet, composed of both a molecular and a weakly ionized component. We can assess if this warm gas represents a dynamically important component of the jet, by measuring its mass flux and comparing it with estimates of the mass flux based on ISO and sub-mm observations of the CO emission (Nisini et al. 2000; Bachiller et al. 1990). We can determine the mass flux for both the molecular and atomic counterparts of the outflow, using as tracers H_2 and [FeII]/[SI] respectively. The method is similar in both cases and is based on the fact that the line emission is optically thin, so that the observed luminosity is proportional to the mass of the emitting gas (Hartigan et al. 1994). For [FeII] and [SI] we have applied the relationship given in Nisini et al. (2005):

¹neutral hydrogen collisional rates for ions, such as [FeII] and [SiII], are about 10^6 times weaker than electron collisional rates: we have checked that n_H collisions start to give comparable ion emissivities with respect to electron collisions only for $n_H > 10^5 \text{ cm}^{-3}$ and $n_e < 500 \text{ cm}^{-3}$. We have therefore not considered collisions with n_H in our calculations of [FeII] and [SiII] emissivities

$$\dot{M} = \mu m_H \times (n_H V) \times (dv_t/dl_t) \quad (2)$$

where μ is the mean atomic weight, m_H is the proton mass, n_H is the total number density, V the volume of the emitting region, dl_t is the projected length perpendicular to the line of sight and dv_t the tangential velocity of the observed region. The number of emitting atoms can be derived from the line luminosity according to the relation:

$$n_H V = L(\text{line}) \left(h\nu A_i f_i \left[\frac{X}{H} \right] \right)^{-1} \quad (3)$$

where A_i and f_i are the radiative rate and fractional population of the upper level, and $[X/H]$ is the gas phase abundance of the considered atom/ion. For the determination of the mass flux from the [FeII]26 μm line, we have assumed that all iron is singly ionized based on the fact that no neutral iron lines are observed within the IRS range; this assumption is based on the fact that the [Fe I] ground transition at 24 μm is not detected in any of our spectra, in spite of its high radiative rate coefficient, comparable to that of the [FeII] ground transition. We have taken the iron gas phase abundance estimated in Sect 3.1 and listed in Table 4. Conversely, to apply the relationship (3) to the [SI]25 μm line, we have assumed that sulfur is all neutral (as discussed in Sect. 3.1) and taken the sulfur solar abundance.

The projected length dl_t was taken equal to the jet length sampled by the width of the LH slit. Finally, the tangential velocity of the outflow was taken equal to 170 km s⁻¹ as derived from the SiO proper motion study by Girart & Acord (2001). Such a velocity, appropriate for the sub-mm jet, may be just a lower limit for the atomic jet velocity, if the latter is associated with a higher velocity inner component. It has been shown however that atomic jets from Class I/II sources have velocities in the range 100-300 km s⁻¹ (Ray et al. 2007, Davis et al. 2003). We therefore believe that our assumption can introduce an uncertainty of at most a factor of two in the mass flux determination. The derived mass flux values using the above method are listed in Table 5. The uncertainty associated with the Fe gas-phase abundance results in an order of magnitude uncertainty in the mass flux determination using the [FeII]26 μm . The determinations from the [SI] line agree with the range of values derived from [FeII] and indicate a mass flux of the order of 1-2 10⁻⁶ M_\odot yr⁻¹ in the CN position, while lower values, of the order of 3-8 10⁻⁷ M_\odot yr⁻¹, are estimated at the bow-shock OF2 position.

The determination of the mass flux from the H₂ component has been measured instead from the total column density for each extracted region as derived from the excitation

diagrams, applying the relationship:

$$\dot{M} = \mu m_H \times (2 N(H_2)A) \times (dv_t/dl_t) \quad (4)$$

where $N(H_2)$ is the total column density and A is the area sampled by the slit. We consider here again the tangential velocity as measured from the SiO proper motion, assuming that it is representative of all the molecular gas. The derived mass flux along the outflow with this method is presented in Table 5. The H_2 mass flux in the central position is about two orders of magnitude lower than the value derived from the atomic lines while in the OF2 position $\dot{M}(H_2)$ is a factor between 2 and 5 lower than $\dot{M}([SI])$. Thus the bulk of the flowing mass is carried out by the atomic jet all along the sampled positions.

A mass flux of the order of $5 \cdot 10^{-6} M_\odot \text{yr}^{-1}$ has been derived within $20''$ of the driving source combining multi-transition CO sub-mm and ISO data (Nisini et al. 2000). This value is only a factor of few larger than the value we derive from atomic lines at the CN position, which suggests that the atomic jet detected by our observations and the warm CO outflows sampled by the ISO and sub-mm observations are dynamically linked. It is also instructive to examine if the atomic jet detected by our Spitzer observations possesses enough momentum to sustain the entrained CO outflow observed at mm wavelength. Bachiller et al. (1990) derived, for the L1448-mm blue-shifted lobe, a momentum flux of the order of $2.6 \cdot 10^{-4} M_\odot \text{km s}^{-1} \text{yr}^{-1}$, assuming an outflow inclination of 70° with respect to the plane of the sky. If we assume momentum conservation for entrainment of the outflow by the jet, and a total jet velocity of 170 km s^{-1} , we derive that the primary jet should possess a mass flux of the order of $1.4 \cdot 10^{-6} M_\odot \text{yr}^{-1}$. This is consistent with the values we infer from the atomic emission, supporting the hypothesis that the detected atomic jet represents the energetically most important component of the outflow.

The accretion rate can be also estimated assuming the bolometric luminosity is mainly due to accretion. Using a stellar mass $M_\star \sim 0.5 M_\odot$ (Froebrich et al. 2003) and a stellar radius $R_\star \sim 4 R_\odot$ (Stahler et al. 1980), we get an accretion rate $\dot{M}_{acc} \sim L_{bol} R_\star / G M_\star \sim 2 \cdot 10^{-6} M_\odot \text{yr}^{-1}$. We thus derive a value comparable to the mass ejection rate estimated above. This is inconsistent with the picture that about only 10% of the mass accreting on the protostar is ejected by means of magneto-centrifugal acceleration mechanisms (e.g. Ferreira et al. 2006). This may indicate that the actual protostellar mass is lower than assumed, and that the source is still at the beginning of its main accretion phase.

6. Conclusions

We have carried out Spitzer IRS spectroscopic observations towards the molecular jet driven by the Class 0 source L1448-C. We have detected the H₂ pure rotational lines from S(0) to S(7) alongside fundamental fine-structure transitions of Si⁺, S⁰ and Fe⁺. Additional UKIRT/UIST spectra have been acquired, showing that, at variance with the 0–0 lines, near-IR H₂ vibrational line emission is mainly confined to the bow shock region where the jet and the ambient molecular cloud interact. We have analysed these lines in order to derive the physical and dynamical parameters of the associated warm gas. The main results can be summarised as follow:

- The detection of the fine-structure lines testify for the presence to a previously unknown atomic jet, embedded in the molecular outflow. An analysis based on the line ratios as well as on previous observations at sub-mm wavelengths indicates that the excitation conditions of this jet are very low. In the region close to the driving source, a temperature $T_e < 1500$ K and an electron density $n_e \sim 200\text{-}1000$ cm⁻³ have been measured, while the estimated ionization fraction is surprisingly $< 10^{-2}$. We suggest that the detected atomic gas represents the analog of the Forbidden Emission Line (FEL) region observed in the more evolved Class I/II sources, although with very different excitation conditions. The close similarity with the FEL region is seen in the decrease of intensity of the atomic emission with distance from the source; in both cases this is likely caused by the expansion of the jet and the consequent gas cool down. Observations with better spatial and spectral resolution, like those that will be possible with the Mid-Infrared Instrument (MIRI) instrument on the James Webb Space Telescope (JWST), are needed to have a better picture of the origin of this gas through comparison with jet acceleration models.
- The H₂ rotational emission indicates the presence of warm gas at a temperature ranging between 600 and 900 K. It is only at the bow shock position that a second component at higher temperature is detected in the near-IR. The H₂ emission in the inner jet region may represent warm molecular gas enveloping the atomic gas: such a molecular component can be also related with the collimated SiO jet observed at sub-mm wavelengths, the excitation conditions of which are similar to those inferred here for the H₂.

At the bow shock position, the near and mid-IR H₂ line observations have been compared with a C-type bow shock model. Shock velocities of ~ 100 km s⁻¹ and pre-shock densities $n(\text{H}_2) \sim 10^5$ cm⁻³ can account rather well for the observed column density.

- The gas phase abundance of Fe and Si has been estimated to infer the amount of

dust reprocessing in the jet. Only a fraction of ~ 0.1 - 0.3 of the solar abundance of Fe and Si is in gaseous form indicating that dust still plays a major role in the depletion of refractory elements. A comparison with the SiO abundance recently derived from the analysis of sub-mm transitions shows that the Si/SiO abundance ratio is ~ 100 , and thus that most of the silicon released from grains by sputtering and grain-grain collisions remains in atomic form. The inferred Fe gas-phase abundance is similar to the values previously estimated in Class I jets by means of near-IR lines: this suggests that dust reprocessing does not depend on evolutionary status of the outflows although further studies are required to confirm this.

- Estimates of the atomic and molecular mass flux rates have been derived from the luminosity of the outflows and the kinematical information given by sub-mm interferometric data. Values of the order of $\sim 10^{-6}$ and $\sim 10^{-7} M_{\odot} \text{ yr}^{-1}$ are inferred from the [SI]25 μm and H₂ line luminosities, respectively. A comparison with the momentum flux of the large scale CO molecular outflow suggests that the detected atomic jet has the power to drive the large scale outflow and thus may represent the primary jet ejected by the source.

The present work was supported in part by the European Communitys Marie Curie Actions - Human Resource and Mobility within the JETSET (Jet Simulations, Experiments and Theory) network under contract MRTN-CT-2004 005592. This work is based on observations made with the Spitzer Space Telescope, which is operated by the Jet Propulsion Laboratory, California Institute of Technology under a contract with NASA, and with the the United Kingdom Infrared Telescope, operated by the Joint Astronomy Centre on behalf of the Science and Technology Facilities Council of the U.K.

REFERENCES

- Asplund, M., Grevesse, N., & Sauval, A. J. 2005, ASPC, 336, 25
- Bachiller, R. Martin-Pintado, J. Tafalla, M. Cernicharo, J., & Lazareff, B. 1990, A&A, 231, 174
- Bachiller, R., Guilloteau, S., Dutrey, A., Planesas, P., & Martin-Pintado, J. 1995, A&A, 299, 857
- Cabrit, S., Codella, C., Gueth, F., Nisini, B., Gusdorf, A., Dougados, C., & Bacciotti, F. 2007, A&A, 468, 29

- Caratti o Garatti, A., Giannini, T., Nisini, B., & Lorenzetti, D. 2006, *A&A*, 449, 1077
- Casse, F., & Ferreira, J. 2000, *A&A*, 353, 1115
- Codella, C., Cabrit, S., Gueth, F., Cesaroni, R., Bacciotti, F., Lefloch, B., & McCaughrean, M. J. 2007, *A&A*, 462, 53
- Davis, C. J., & Smith, M. D. J. 1996, *A&A*, 309, 929
- Davis, C. J., Whelan, E., Ray, T. P., & Chrysostomou, A. 2003, *A&A*, 397, 693
- Dufton, P. L., & Kingston, A. E. 1991, *MNRAS*, 248, 827
- Enoch, M. L., Young, K. E., Glenn, J., & Evans, N. J. II et al. 2006, *ApJ*, 638, 293
- Ferreira, J., Dougados, C., & Cabrit, S. 2006, *A&A*, 453, 785
- Froebrich, D., Smith, M. D., & Eislöffel, J. 2002, *A&A*, 385, 239
- Froebrich, D., Smith, M. D., & Eislöffel, J. 2003, *Ap&SS*, 287, 217
- Giannini, T., Nisini, B., & Lorenzetti, D. 2001, *ApJ*, 555, 40
- Giannini, T., Calzoletti, L., Nisini, B., Davis, C. J., Eislöffel, J., & Smith, M. D. 2008, *A&A*, 481, 123
- Gibb, A. G., Davis, C. J., & Moore, T. J. T. 2007, *MNRAS*, 382, 1213
- Girart, J. M., & Acord, J. M. P. 2001, *ApJ*, 552, 63
- Gorti, U., & Hollenbach, D. 2008, *ApJ*, in press
- Gueth, F. & Guilloteau, S. 1999, *A&A*, 343, 571
- Guilloteau, S., Bachiller, R., Fuente, A., & Lucas, R. 1992, *A&A*, 265, 49
- Gusdorf, A., Cabrit, S., Flower, D. R., & Pineau Des Forêts, G. 2008, *A&A*, 482, 809
- Hartigan, P., Morse, J. A., & Raymond, J. 1994, *ApJ*, 436, 125
- Higdon S. J. U. et al. 2004, *Astr. Soc. Pacific* 116, 975
- Hollenbach, D., & McKee, C. F. 1989, *ApJ*, 342, 306
- Houck, J., et al. 2004, *ApJS*, 154, 18
- Jones, A. P. 2000, *J. Geophys. Res.*, 105, 10257

- Jørgensen, J. K. et al. 2006, *ApJ*, 645, 1246
- Königl, A., & Pudritz, R. E. 2000, *Protostars to Planets V*, 759
- Lahuis, F., van Dishoeck, E. F., Blake, G. A., Evans, N. J. II, Kessler-Silacci, J. E., & Pontoppidan, K. M. 2007, *ApJ*, 665, 492
- Landini, M., & Monsignori Fossi, B. C. 1990, *A&AS*, 82, 229
- Lee, C.-F., Ho, P. T. P., Palau, A., Hirano, N., Bourke, T. L., Shang, H., & Zhang, Q. 2007, *ApJ*, 670, 1188
- Mathis, J. S. 1998, *ApJ*, 497, 824
- Nisini, B., Benedettini, M., Giannini, T., Caux, E., di Giorgio, A. M., Liseau, R., Lorenzetti, D., Molinari, S., Saraceno, P., Smith, H. A., Spinoglio, L., & White, G. J. 1999, *A&A*, 350, 529
- Nisini, B., Benedettini, M., Giannini, T., Codella, C., Lorenzetti, D., di Giorgio, A. M., & Richer, J. S. 2000, *A&A*, 360, 297
- Nisini, B., Caratti o Garatti, A., Giannini, T., & Lorenzetti, D. 2002, *A&A*, 393, 1035
- Nisini, B., Bacciotti, F., Giannini, T., Massi, F., Eislöffel, J., Podio, L., & Ray, T. P. 2005, *A&A*, 441, 159
- Nisini, B., Codella, C., Giannini, T., Santiago Garcia, J., Richer, J. S., Bachiller, R., & Tafalla, M. 2007, *A&A*, 462, 163
- Pascucci, I., et al. 2007, *ApJ*, 663, 383
- Podio, L., Bacciotti, F., Nisini, B., Eislöffel, J., Massi, F., Giannini, T., & Ray, T. P. 2006, *A&A*, 456, 189
- Ray, T., Dougados, C., Bacciotti, F., Eislöffel, J., & Chrysostomou, A. 2007, *Protostars to Planets V*, 231
- Rieke, G. H., & Lebofsky, M. J. 1985, *ApJ*, 228, 618
- Takami, M., Chrysostomou, A., Ray, T. P., Davis, C., Dent, W. R. F., Bailey, J., Tamura, M., & Terada, H. 2004, *A&A*, 416, 213
- Tobin, J. J., Looney, L. W., Mundy, L. G., Kwon, W., & Hamidouche, M. 2007, *ApJ*, 659, 1404

- Schilke, P., Walmsley, C. M., Pineau des Forêts, G., & Flower, D. R. 1997, *A&A*, 321, 293
- Stahler, S. W., Shu, F. H., & Taam, R. E. 1980, *ApJ*, 241, 637
- Stancil, P. C., Havener, C. C., Krstic, P. S., Schultz, D. R., Kimura, M., Gu, J.-P., Hirsch, G., Bunker, R. J., & Zygelman, B. 1998, *ApJ*, 502, 1006
- Smith, M. D. 1991, *MNRAS*, 252, 378
- Whittet, D. C. B., Shenoy, S. S., Bergin, E. A., Chiar, J. E., Gerakines, P. A., Gibb, E. L., Melnick, G. J., & Neufeld, D. A. 2007, *ApJ*, 655, 332

Table 1. L1448 observed lines:SPITZER/IRS

Lines			$F \pm \Delta F (10^{-14} \text{erg cm}^{-2} \text{s}^{-1})$			
$\lambda(\mu\text{m})$	Element(Transition)	Module	CS	CN	OF1	OF2
5.51116	H ₂ 0-0 S(7)	SL	5.5±1.5	4.5±0.1	3.8±0.6	3.9±0.2
6.10856	H ₂ 0-0 S(6)	SL	< 0.7	2.1±0.5	1.7±0.3	4.8±0.9
6.90952	H ₂ 0-0 S(5)	SL	3.2±1.0	7.8±0.6	6.4±0.6	9.3±0.5
8.02505	H ₂ 0-0 S(4)	SL	< 2	7.0±1.5	2.8±0.7	4.5±0.2
9.66491	H ₂ 0-0 S(3)	SL	< 0.5	4.9±0.7	10.8±2.2	20.1±0.3
12.2786	H ₂ 0-0 S(2)	SL	1.1±0.4	2.8±0.7	3.5±0.4	4.0±0.4
12.2786	H ₂ 0-0 S(2)	SH	1.7±0.2	2.9±0.2	3.3±0.2	8.4±0.3
17.0348	H ₂ 0-0 S(1)	SH	0.4±0.1	2.4±0.1	3.2±0.2	5.7±0.1
28.2188	H ₂ 0-0 S(0)	LH	< 0.6	< 1	1.2±0.4	2.1±0.3
5.33042	H ₂ 1-1 S(8)	SL	< 0.8	< 2	< 1.3	< 2
5.81112	H ₂ 1-1 S(7)	SL	< 0.8	< 1	< 1	< 1.6
6.43710	H ₂ 1-1 S(6)	SL	< 1.3	< 1.7	< 1.2	< 1.8
7.28070	H ₂ 1-1 S(5)	SL	< 2	< 1.6	< 1.5	< 0.9
8.45367	H ₂ 1-1 S(4)	SL	< 1.2	< 0.8	< 0.5	< 0.8
10.1777	H ₂ 1-1 S(3)	SL	< 0.5	< 0.8	< 0.9	< 0.8
12.9275	H ₂ 1-1 S(2)	SL	< 0.8	< 0.5	< 0.8	< 1.8
17.9320	H ₂ 1-1 S(1)	SH	< 0.5	< 0.6	< 0.4	< 0.4
29.7017	H ₂ 1-1 S(0)	LH	< 2	< 2	< 0.9	< 0.8
5.34017	[FeII] ⁴ F _{9/2} – ⁶ D _{9/2}	SL	< 2	< 1	< 2	< 3
17.9359	[FeII] ⁴ F _{7/2} – ⁴ F _{9/2}	SH	< 0.4	< 0.3	< 0.5	< 0.4
25.9883	[FeII] ⁶ D _{7/2} – ⁶ D _{9/2}	LH	< 1	9.7±0.4	1.2±0.1	4.2±0.1
35.7774	[FeII] ⁴ F _{3/2} – ⁴ F _{5/2}	LH	< 2	< 3	< 3	< 1.5
25.2490 ^a	[SI] ³ P ₁ – ³ P ₂	LH	5.8±0.3	15.2±0.5	3.2±0.2	6.8±0.2
25.2490	[SI] ³ P ₁ – ³ P ₂	LH	5.3±0.4	19.2±0.5	2.6±1.2	6.1±0.2
34.8152	[SiII] ² P _{3/2} – ² P _{1/2}	LH	< 8	12.9±4.2	< 3	5.6±0.6

^athe [SI]25.2 μm line is detected in two different orders of the LH module.

Table 2. L1448 observed lines:UKIRT/UIST

Lines		$F \pm \Delta F(10^{-16}\text{erg cm}^{-2} \text{s}^{-1})$		
$\lambda(\mu\text{m})$	Element(Transition)	CN	OF1	OF2
1.6877	H ₂ 1-0 S (9)	< 0.3	< 0.04	0.15±0.03
1.7147	H ₂ 1-0 S (8)	< 0.4	< 0.05	0.17±0.04
1.7480	H ₂ 1-0 S (7)	< 0.4	< 0.05	0.94±0.05
1.7880	H ₂ 1-0 S (6)	< 0.4	< 0.05	0.75±0.05
1.9576	H ₂ 1-0 S (3)	<0.3	0.52±0.05	8.10±0.04
2.0338	H ₂ 1-0 S (2)	1.36±0.45	0.29±0.04	2.65±0.05
2.0735	H ₂ 2-1 S (3)	< 0.5	< 0.06	1.00±0.05
2.1218	H ₂ 1-0 S (1)	3.51±0.33	1.00±0.05	7.90±0.04
2.1542	H ₂ 2-1 S (2)	< 0.4	< 0.05	0.38±0.05
2.2235	H ₂ 1-0 S (0)	< 0.4	0.35±0.05	2.10±0.06
2.2477	H ₂ 2-1 S (1)	< 0.4	< 0.05	0.97±0.04
2.3556	H ₂ 2-1 S (0)	< 0.3	< 0.04	0.32±0.04
2.4066	H ₂ 1-0 Q (1)	8.07±0.39	1.31±0.04	9.73±0.04
2.4134	H ₂ 1-0 Q (2)	3.28±0.36	0.45±0.05	4.10±0.03
2.4237	H ₂ 1-0 Q (3)	8.01±0.37	1.56±0.05	9.86±0.04
2.4375	H ₂ 1-0 Q (4)	1.49±0.28	0.42±0.05	2.59±0.06
2.4548	H ₂ 1-0 Q (5)	5.89±0.30	1.09±0.05	5.34±0.04
2.4756	H ₂ 1-0 Q (6)	< 0.4	< 0.05	1.75±0.05
2.5001	H ₂ 1-0 Q (7)	< 0.5	< 0.06	3.56±0.06

Table 3. Temperatures and Column Densities

Position	H ₂		FeII / SiII	
	T(K)	N(H ₂) (cm ⁻²)	T(K)	n _e (cm ⁻³)
CS	900±170	3.18 10 ¹⁷
CN	755±35	7.81 10 ¹⁷	<1700	200-1000
OF1	600±30	1.92 10 ¹⁸
OF2	670±50	2.34 10 ¹⁸	<2500	300-500

Table 4. Gas-phase abundance of Fe and Si

Position	CN	OF1	OF2
$[Fe_{gas}]/[Fe_{\odot}]^a$	$3-5 \cdot 10^{-2}$	$4-7 \cdot 10^{-2}$	$3-5 \cdot 10^{-2}$
$[Fe_{gas}]/[Fe_{\odot}]^b$	$1-2 \cdot 10^{-1}$	$1.5-3 \cdot 10^{-1}$	$1-2 \cdot 10^{-1}$
$[Si_{gas}]/[Si_{\odot}]^a$	$3-5 \cdot 10^{-2}$...	$3-5 \cdot 10^{-2}$
$[Si_{gas}]/[Si_{\odot}]^b$	$1-2 \cdot 10^{-1}$...	$1-2 \cdot 10^{-1}$

^a assuming collisions with electrons and $n_e = 400 \text{ cm}^{-3}$

^b assuming collisions with n_H , $n_{tot} = 10^5 \text{ cm}^{-3}$ and $n_H = 0.1 n_{tot}$

Table 5. Physical parameters

Position	$\dot{M}(\text{H}_2)$	$\dot{M}([\text{SI}])$	$\dot{M}([\text{FeII}])$
	$(10^{-7} M_{\odot} \text{ yr}^{-1})$		
CN	0.5	9–20	2–20
OF2	1.4	3–8	0.9–9

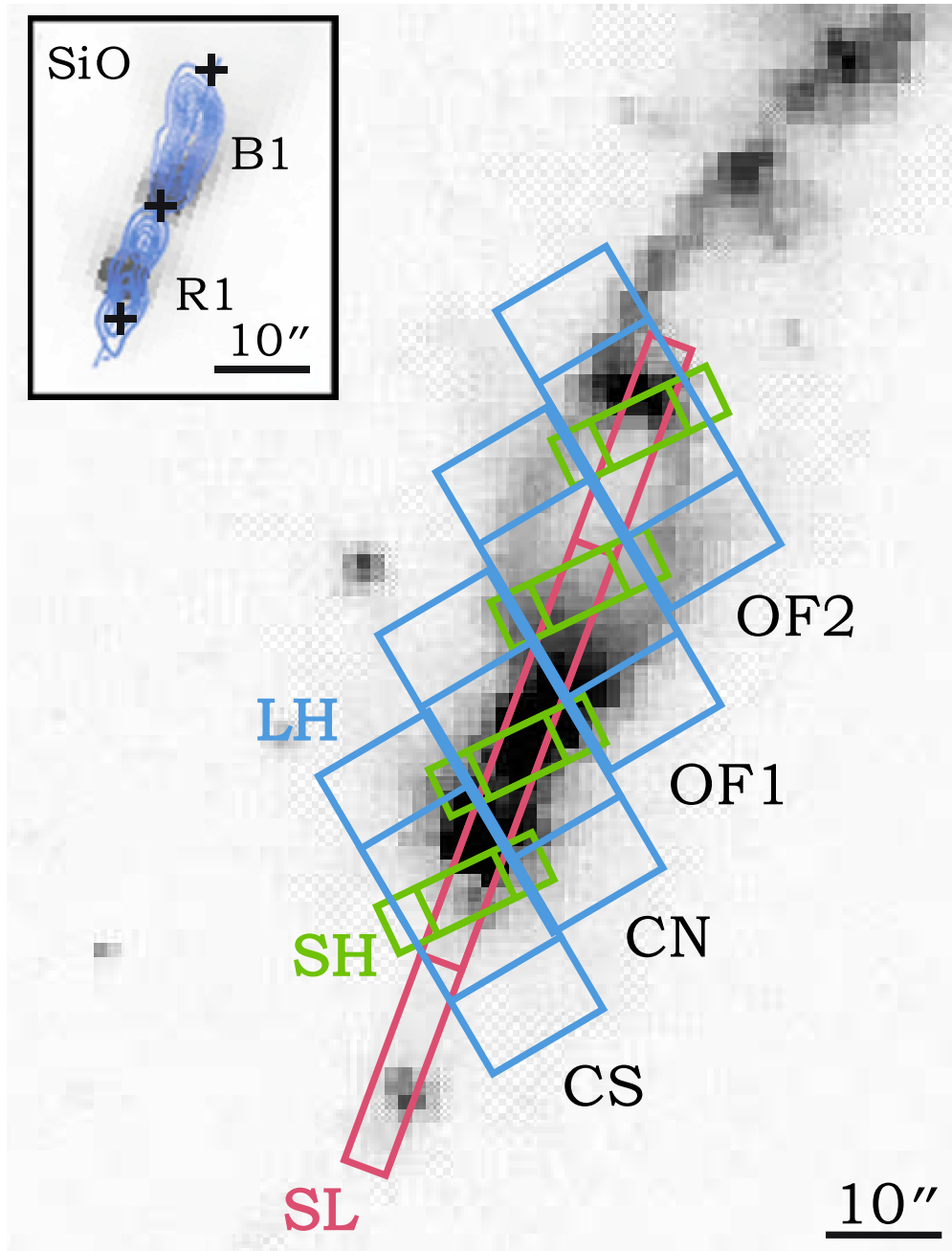


Fig. 1.— Positioning of IRS slits for the SL, SH, & LH modules, overlaid on 4.5 μm IRAC image (from the c2d survey). For the SL and LH modules, both nodding positions are displayed, whereas for the SH module only the outline of the observed area is presented for clarity. The intersections of the slits define four areas of extraction along the jet axis. (*Upper left*) SiO (Guilloteau et al. 1992) contours overlaid on the 4.5 μm image show that the driving source is almost coincident with the northern emission area; crosses indicate the centers of the CS, CN and OF1 positions from bottom to top.

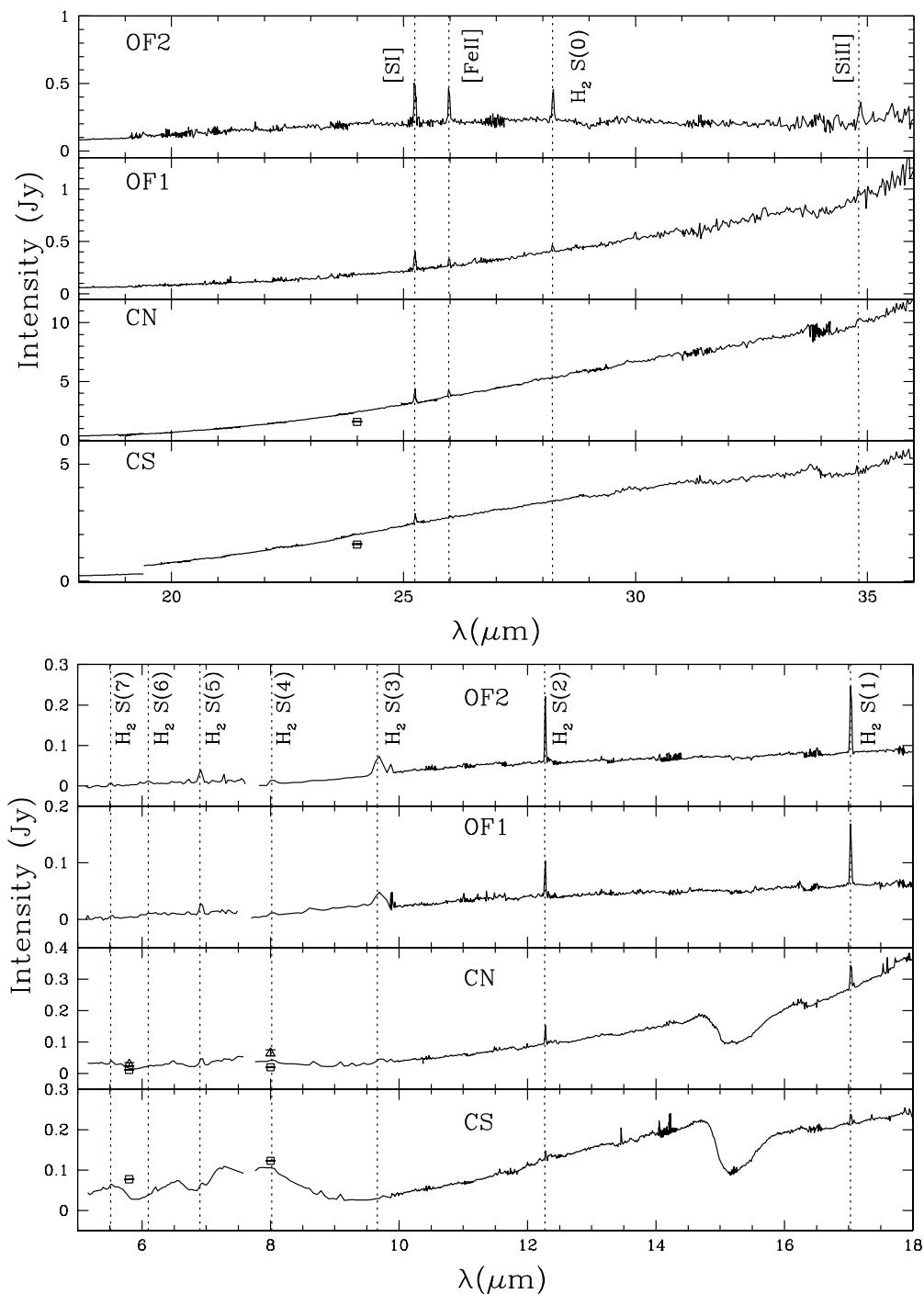


Fig. 2.— Extracted spectra (*lower panel: 5 - 18 μm , upper panel: 18 - 38 μm*) for each of the four positions defined in Figure 1, after defringing and removing zodiacal light. The observed lines are labeled on the top of each set. Open squares and triangles are IRAC bands 3,4 and MIPS band 1 continuum flux measurements from Jørgensen et al. (2006) and Tobin et al. (2007).

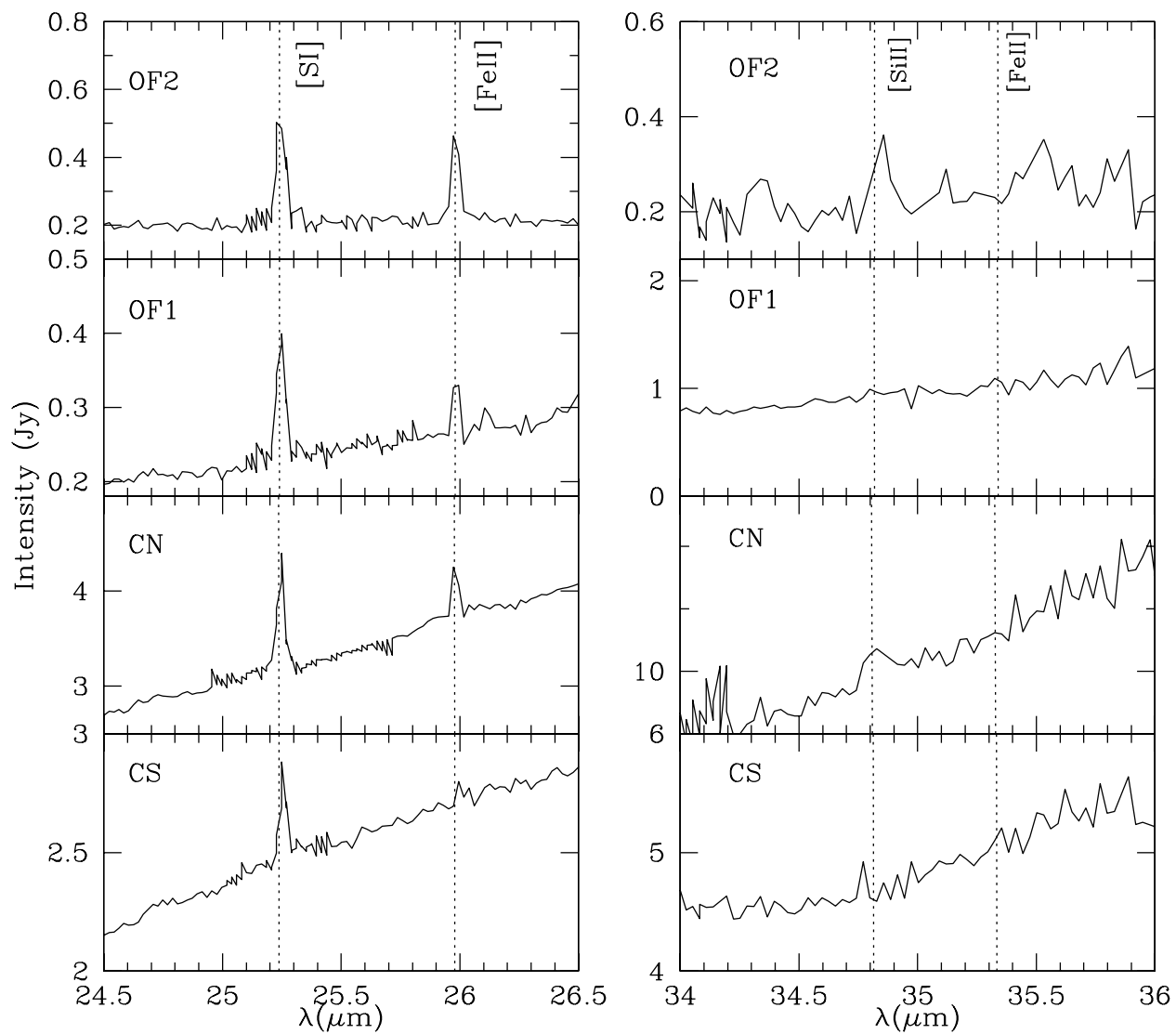


Fig. 3.— Magnification of the spectra presented in Fig.2 displaying the ionic lines.

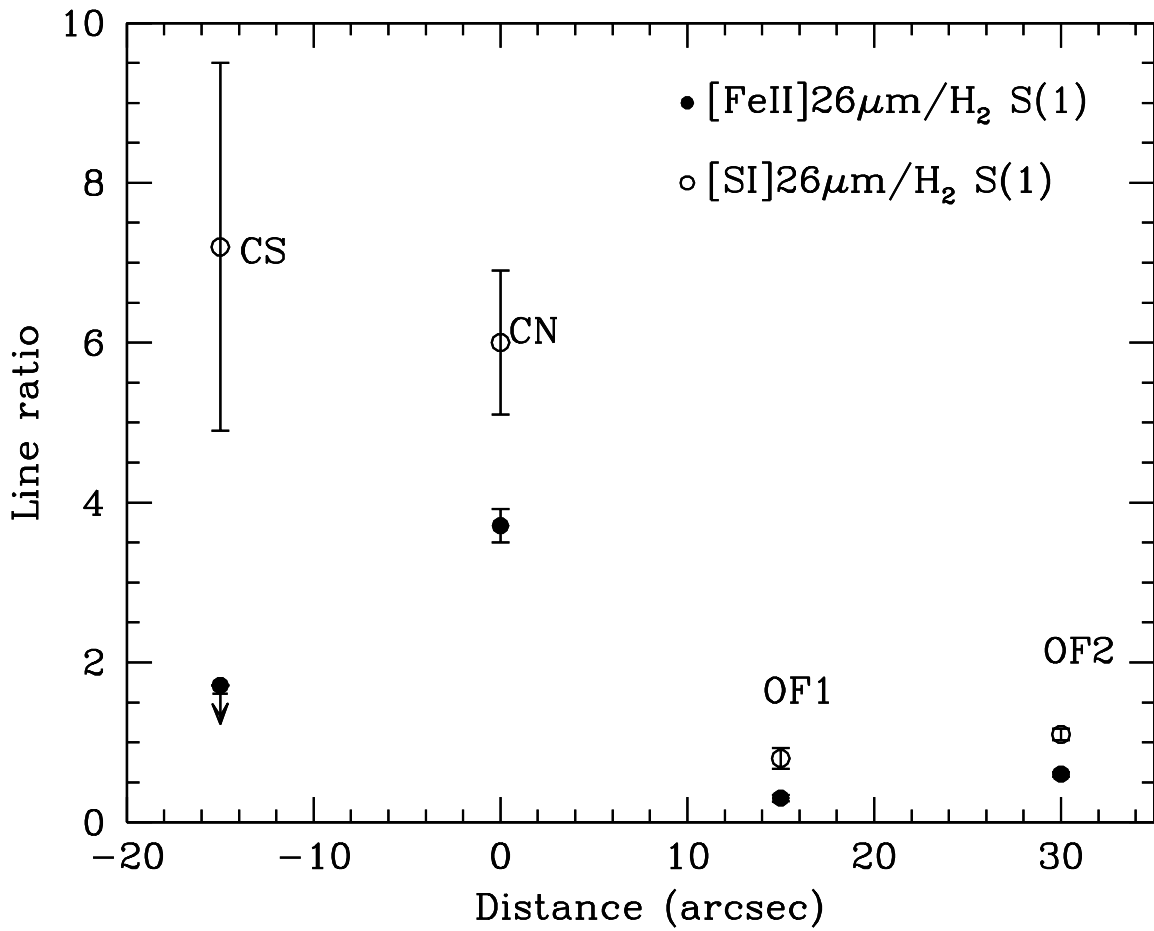


Fig. 4.— Ratio of the atomic ([FeII]26μm and [SI]25μm) over the molecular (H₂ S(1)) line emission. Atomic emission dominates close to the driving source (CN) while the atomic/molecular contribution decreases in the OF1 and OF2 positions (see Fig. 1).

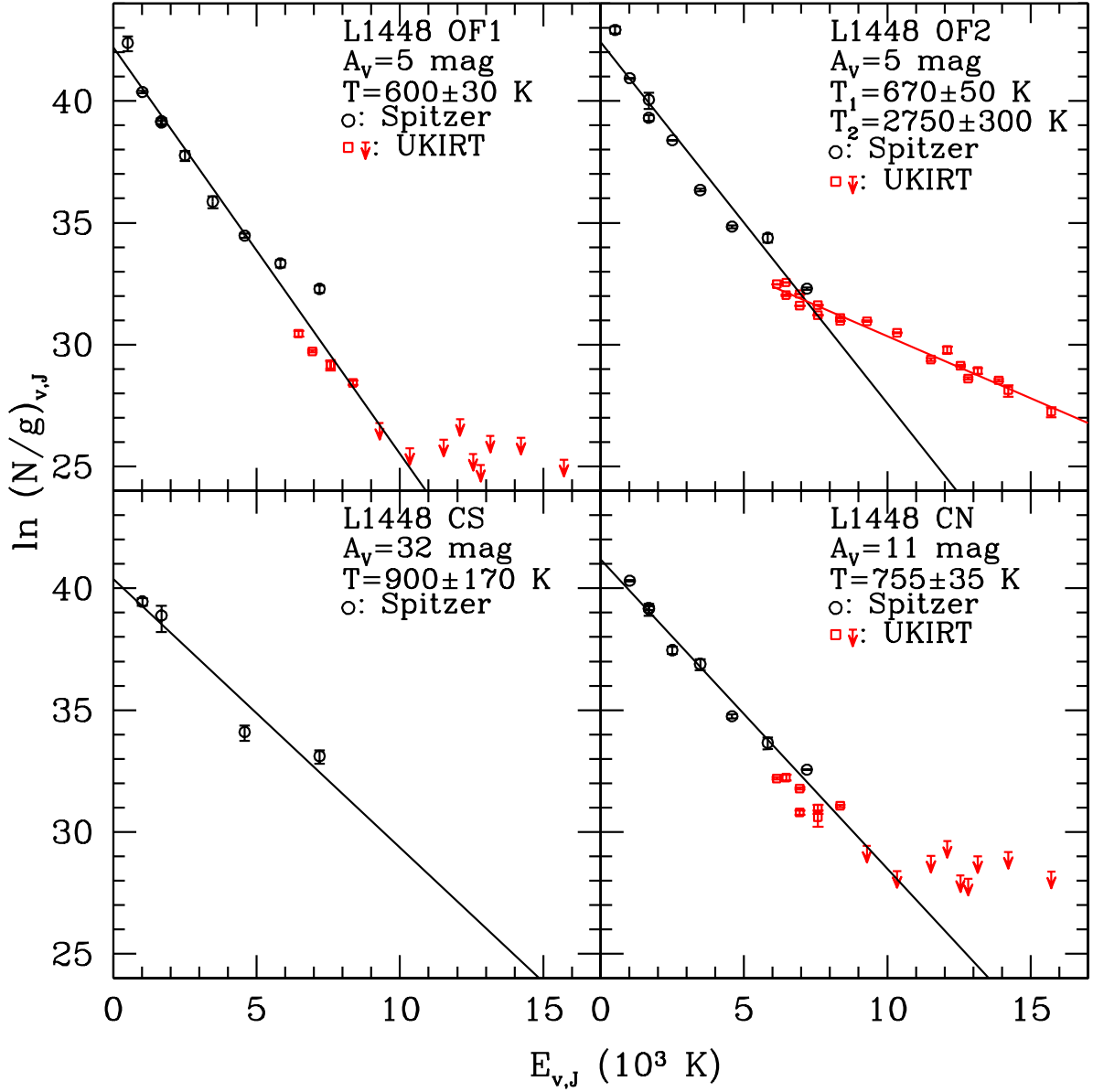


Fig. 5.— Excitation diagram of the H_2 lines for each position defined in Fig. 1. Spitzer (open circles) and UKIRT (open squares and arrows for the upper limits) data points are optimally least square fitted (solid line). Temperatures and total column densities are derived from the slope of the fitted line, and its intersection with the $\ln(N_{v,J}/g)$ axis. Visual extinction values used for dereddening and derived temperatures are displayed in the upper left corner of each panel.

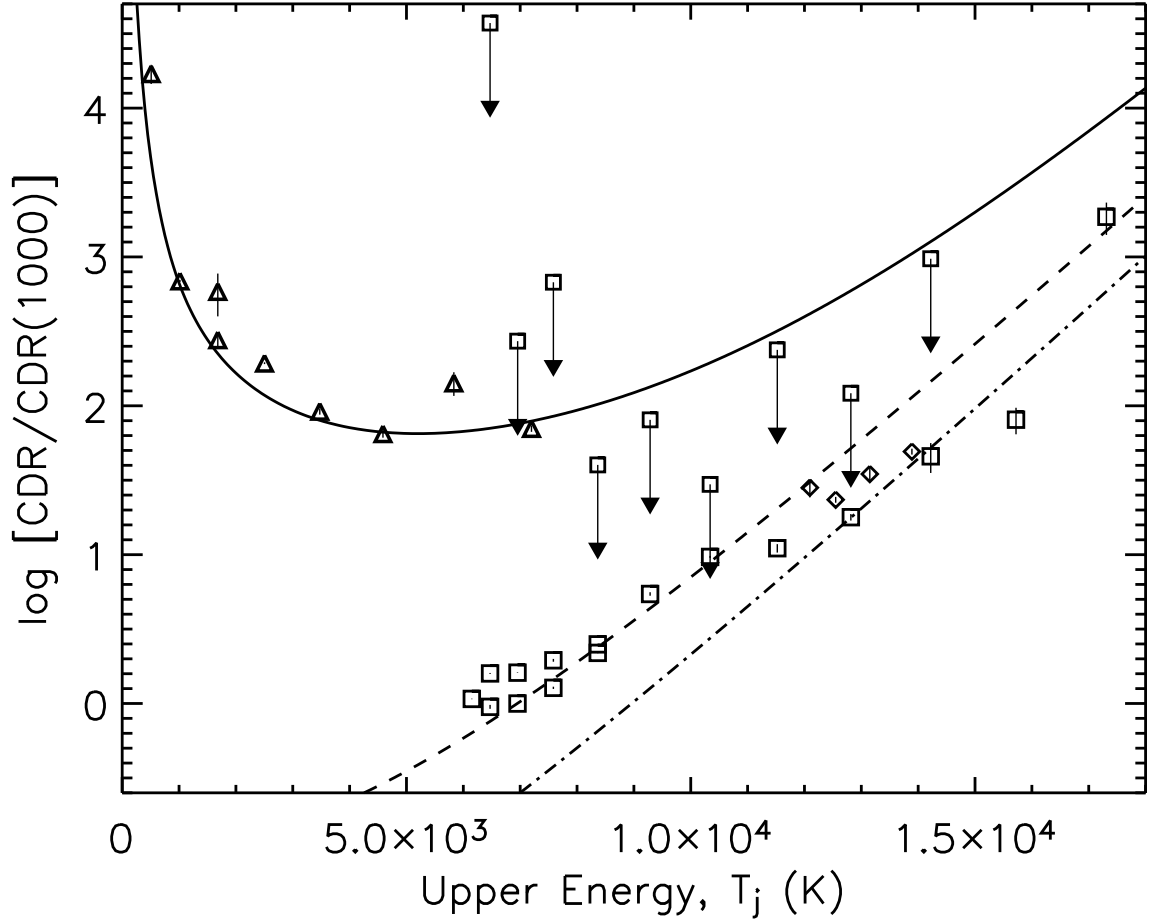


Fig. 6.— Column Density Ratio (CDR) diagram of the OF2 position, constructed normalising the column density of each transition to the value given by a gas at 1000K and to the 1–0 S(1) column density. Triangles represent Spitzer 0–0 lines, squares represent lines from the first vibrational levels, including the 1–1 upper limits derived from the Spitzer IRS spectra, and diamonds correspond to 2–1 S lines. The superimposed model predictions are for the ground (solid), first (dashed) and second (dot-dashed line) vibrational level. The fit corresponds to a bow shock moving at 100 km s^{-1} into a medium of total density 10^5 cm^{-3} .

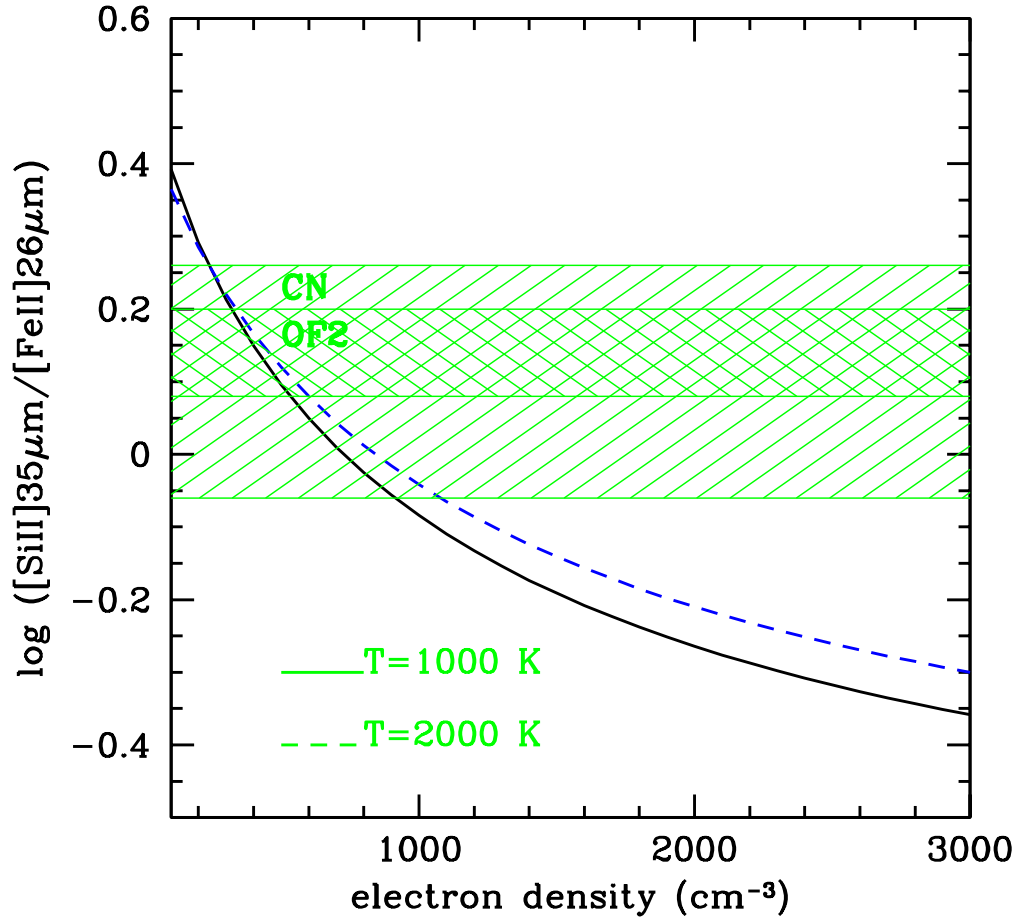


Fig. 7.— Diagnostic diagram of the $[\text{SiII}]_{35\mu\text{m}}/[\text{FeII}]_{26\mu\text{m}}$ ratio versus electron density, for temperatures of 1000K and 2000K (solid and dashed lines). Hatched areas represent the observed ratio for the CN and OF2 regions that correspond to electron densities of from 200 to 1000 cm^{-3} and from 300 to 500 cm^{-3} respectively.

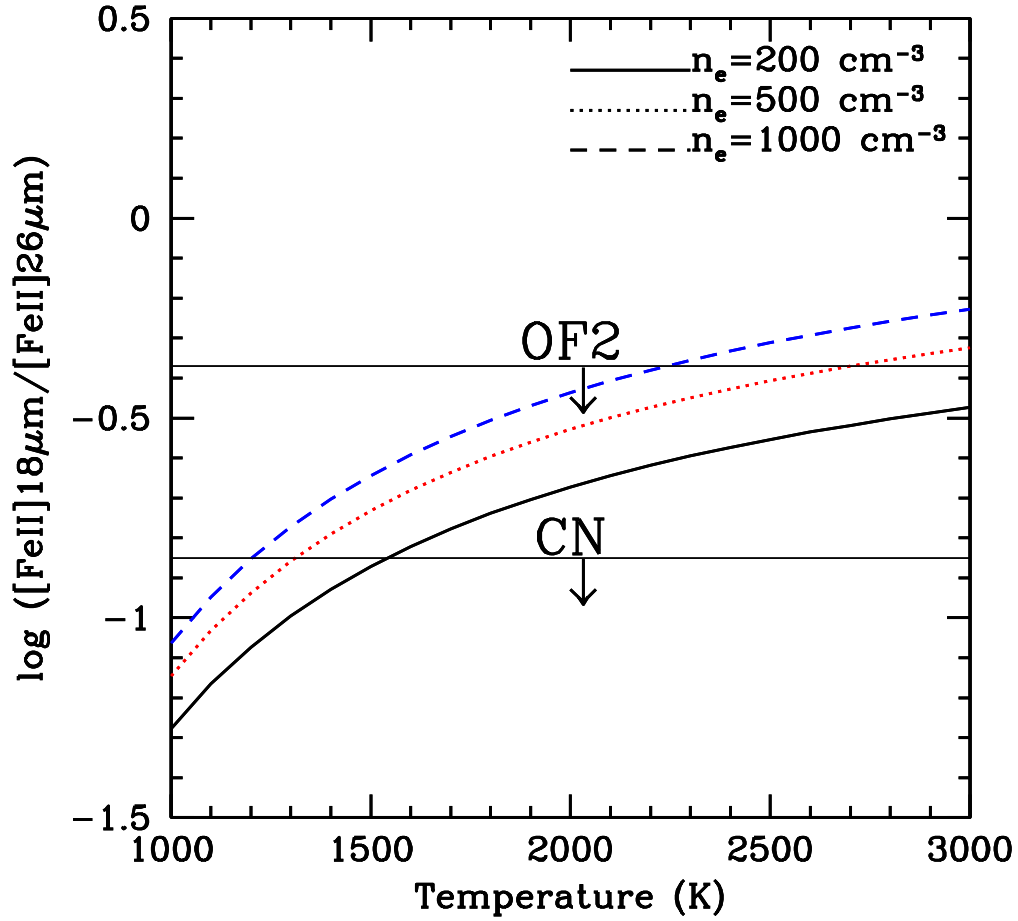


Fig. 8.— Diagnostic diagram of $[\text{FeII}]_{18\mu\text{m}}/[\text{FeII}]_{26\mu\text{m}}$ ratio versus temperature, for electron densities of $2 \cdot 10^2$, $5 \cdot 10^2$ and 10^3 cm^{-3} (solid and dashed lines respectively). The non-detection of the $[\text{FeII}]_{18\mu\text{m}}$ line allows us only to constrain the upper temperature limits for the CN and OF2 positions